Operando surface chemistry of micro- and nanocubic copper catalysts for electrochemical CO$_2$ reduction

Karla Banjac[1,2]*, Thanh Hai Phan[1,2], Fernando P. Cometto[1], Patrick Alexa[3], Yunchang Liang[1,2], Rico Gutzler[3], and Magalí Lingenfelder[1,2]*.

[1] Max Planck-EPFL Laboratory for Molecular Nanoscience and Technology, Ecole Polytechnique Fédérale de Lausanne (EPFL), 1015 Lausanne, Switzerland.

[2] Institut of Physics (IPHYS), Ecole Polytechnique Fédérale de Lausanne (EPFL), 1015 Lausanne, Switzerland.

[3] Max Planck Institute for Solid State Research, 70569 Stuttgart, Germany.

e-mails: karla.banjac@epfl.ch, magali.lingenfelder@epfl.ch

Abstract

The electrochemical reduction of CO_2 (CO_2RR) into multicarbon compounds is a promising pathway towards renewable chemicals. Structure-product selectivity studies highlight that copper (100) facets favour C_{2+} product formation. However, the atomic processes leading to the formation of (100)-rich Cu cubes remains elusive. Herein, we use Cu and graphene-protected Cu surfaces to reveal the differences in structure and composition of common Cu-based electrocatalysts, from nano to micrometer scales. We show that stripping/electrodeposition cycles lead to thermodynamically-controlled growth of Cu_2O micro/nanocubes, while multi-layered Cu nanocuboids form universally during CO_2RR upon polarization-driven re-organization of Cu^0 atoms. A synergy of electrochemical characterization by scanning tunnelling microscopy (EC-STM), *operando* EC-Raman and quasi-*operando* X-Ray Photoemission spectroscopy (XPS) allows us to shed light on the role of oxygen on the dynamic interfacial processes of Cu, and to demonstrate that chloride is not needed for the stabilization of cubic Cu nanostructures.

Introduction

The electrochemical reduction of carbon dioxide (CO_2RR) holds promise for the production of renewable fuels and chemicals[1]. Extensive material screening conducted over the last three decades reveals that copper is the best suited element capable of converting CO_2 to hydrocarbons[2–4]. Single crystal studies established the relationship between the structure and CO_2RR product selectivity showing that Cu(100) facets are selective towards ethylene production[5]. Similar product selectivity was found for cube-shaped Cu nanoparticles, *i.e.*, nanocubes with lateral size dimensions between several dozens of nanometres up to several micrometers[6]. The geometry of {100} planes and {110} edges greatly facilitates C–C bond formation towards C_{2+} products[6,7]. This structure-product selectivity relationship is especially viable for ethylene used as a precursor for plastics and ethylene glycol[1], both yet to be produced through a carbon-neutral pathway.

One of the main obstacles towards economically feasible CO_2RR is the poor understanding of the reaction steps and complex processes occurring at the electrochemical interfaces during CO_2RR. In a simple picture, both the electrode and the electrical double layer (EDL) are considered static; however, the latest literature reports that dynamic rearrangements of the electrode surface[8] and EDL[9,10] significantly change local reaction environments[11]. Such surface processes significantly change the initial morphologies of both Cu surfaces and Cu-based nanoparticles (NP). *Operando* electrochemical scanning tunnelling microscopy (EC-STM) studies reveal that Cu-based catalysts enrich in Cu(100) facets (multi-layered nanocuboids or mounds) during CO_2RR/HER, both in the absence[12,14] and the presence[12,13,14] of CO_2. Simultaneously, NPs undergo structural evolutions at the micrometre scale: shape transformations[15] and degradation through a combination of nanoclustering and coalescence[16].

Structural evolutions occurring over both atomistic and micrometre scales[17] underline the importance of tackling the open questions on Cu electro-catalysis through a combination of surface science techniques. A synergy of electrochemical characterization, *operando* spectroscopies and

2

microscopies thus provides an insight into the complex interfacial processes over different lateral and depth scales, while simultaneously overcoming resolution and detection limits inherent to each individual technique[18]. *In-situ* characterization is especially important for Cu catalysts due to their tendency to undergo rapid oxidation. The direct visualization of structural transformations at the atomic scale is possible by using scanning probe microscopies (SPM)[19]. High lateral resolution characteristic for SPM is compromised by the fact that only local reaction environments (surface areas < 5 μm at reasonable scan rates) can be imaged. Alternatively, scanning electron microscopy (SEM) and Transmission electron microscopy (TEM) is greatly used for NP characterization, but suffer from beam-induced damage, and NP shape loss due to oxidation processes.

Cu catalysts rich in (100) facets can be prepared upon nanostructuring polycrystalline Cu surfaces: either through *in situ* emergence of nanocuboids during CO_2RR[12] or through oxidative-reductive cycling[20,21]. While nanocuboid formation has recently been reported as the main morphological evolution during CO_2RR[12,22], micro/nanocubes prepared upon cycling have been widely employed as CO_2RR catalysts[23,21,24,25]. The cycling protocols employ chloride-containing electrolytes, assuming that the cube precursor is CuCl. Cubic CuCl, presumed to be formed during the anodic scan, converts to Cu_2O NCs[20,21]. This hypothesis on CuCl-to-Cu_2O NC transformation, while being valid for CuCl NP precipitation in liquid-phase Cu_2O NCs synthesis based on a hydrolysis approach[26], disagrees with the fact that chloride anions enhance anodic Cu dissolution during cycling.

Here, we report on the differences between micro/nanocubes and nanocuboids formed *in situ* during CO_2RR upon surface nanostructuring. To gain information on their morphologies and chemical compositions, we use a combination of microscopies (SEM, AFM, EC-STM) with *operando* EC-Raman (deep-surface sensitive) and X-ray photoelectron (near-surface sensitive) spectroscopy studies. Our results establish that the emergence of nanocuboids during CO_2RR is a general phenomenon on Cu catalysts due to the potential-driven re-organization of metallic Cu atoms. Moreover, we show that the cubic morphology is inherent to cycling protocols that lead to Cu dissolution in the anodic scan

3

and subsequent electrodeposition in the cathodic scan. Our findings clarify the role of oxygen for stabilization of the microscopic cubic morphology and discard the hypothesis that chloride is needed as a precursor. This study highlights the importance of combined surface science studies for detangling the complex interfacial processes occurring on Cu during CO_2RR and thus, offers a novel outlook for synthesis optimization and stability issues related to Cu(100)-rich catalysts.

Results

**Morphology of nanocuboids *versus* micro/nanocubes**
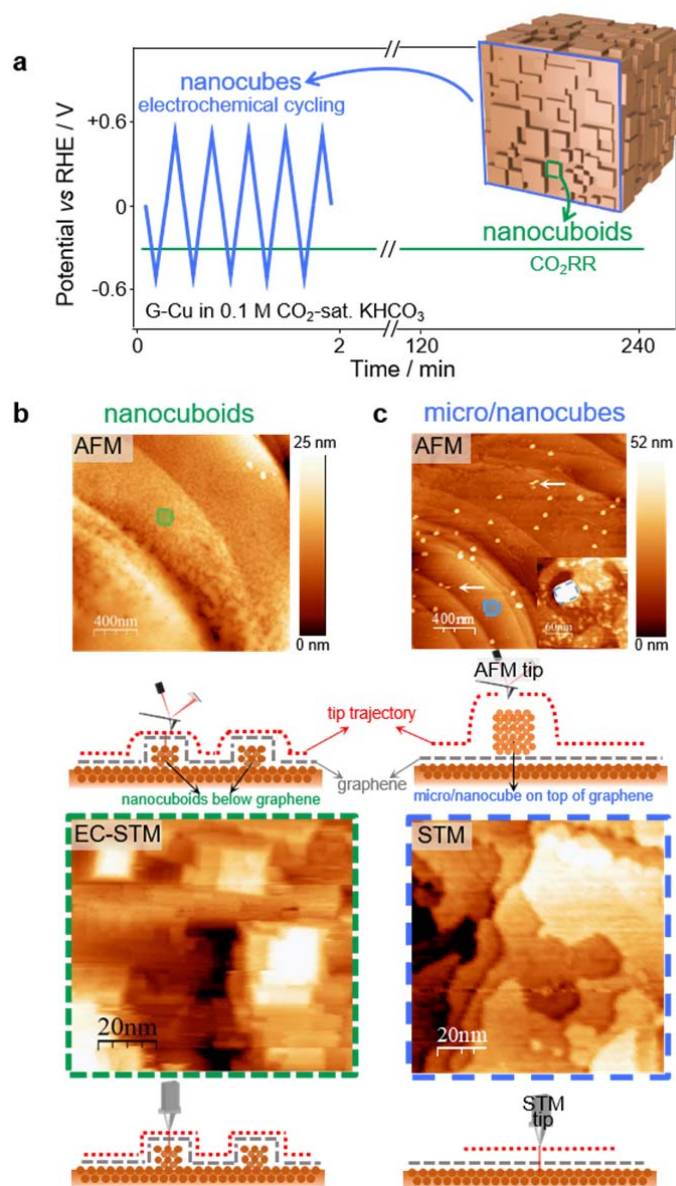
Figure 1. Morphology of Cu-based nanocuboids and micro/nanocubes prepared by electrosynthesis: nanostructuring *versus* electrochemical cycling. a, Constant-potential polarization of g-Cu at -1 V *vs* Pt pseudo-reference electrode and electrochemical cycling of g-Cu between -0.6 V and +0.6 V *vs* RHE in 0.1 M CO_2 saturated $KHCO_3$. **b**, AFM and EC-STM images of the nanocuboids prepared upon surface reconstruction on g-Cu together with the corresponding schemes. **c**, Top panel: AFM height image of Cu_2O nanocubes formed upon cycling. The white arrows denote the scan lines in which NCs were picked up by the AFM tip. Bottom panel: STM image showing the polycrystalline Cu underneath G- after cycling up to +0.9 V *vs* RHE in 0.1 M CO_2 saturated $KHCO_3$. The regions marked on AFM images with the squares are superimposed to highlight the size differences between AFM and STM images.

To study the early stages of the Cu cubic feature formation, we used both polycrystalline pristine Cu

foils (Cu), and Cu covered by a monolayer of graphene (g-Cu, see Methods for details) that have a

5

similar product selectivity for CO_2RR. [12] As the role of oxides on Cu during CO_2RR is under debate[12,27–31], g-Cu was chosen because graphene acts as a protection layer towards air oxidation[32] allowing us to spectroscopically distinguish the differences in chemical composition between the Cu micro/nanocubes on top of graphene and the underlying Cu substrate, which remains mostly metallic upon electrochemical/air oxidation. Moreover, its flatness and well-defined electronic structure facilitates high-resolution SPM characterization (Supplementary Fig. 1). In the case of EC-STM, we have recently shown that one can scan preferentially the same region either on top or underneath graphene, by finding the bias conditions where graphene is transparent to STM[12].

Figure 1 compares the morphologies of the nanocuboids synthetized on g-Cu upon constant-potential polarization and the micro/nanocubes prepared upon cycling. Nanocuboids were formed upon constant-potential polarization of g-Cu in 0.1 M CO_2 saturated $KHCO_3$ (**Figure 1**.b)[12]. AFM images of as-treated g-Cu show that the initial flat Cu surface (Supplementary Fig. 1) became 'granular', similar to the uncovered Cu surfaces reported by Arán-Ais *et al*[33]. High-resolution EC-STM images of the Cu surface underneath graphene reveal that the nanocuboids are (100) facet multilayers. For g-Cu, graphene remained intact during surface evolution (Supplementary Fig. 2). As a result, nanocuboids were covered by graphene, and no nanoparticles are found on top of graphene (Figure 1.a).
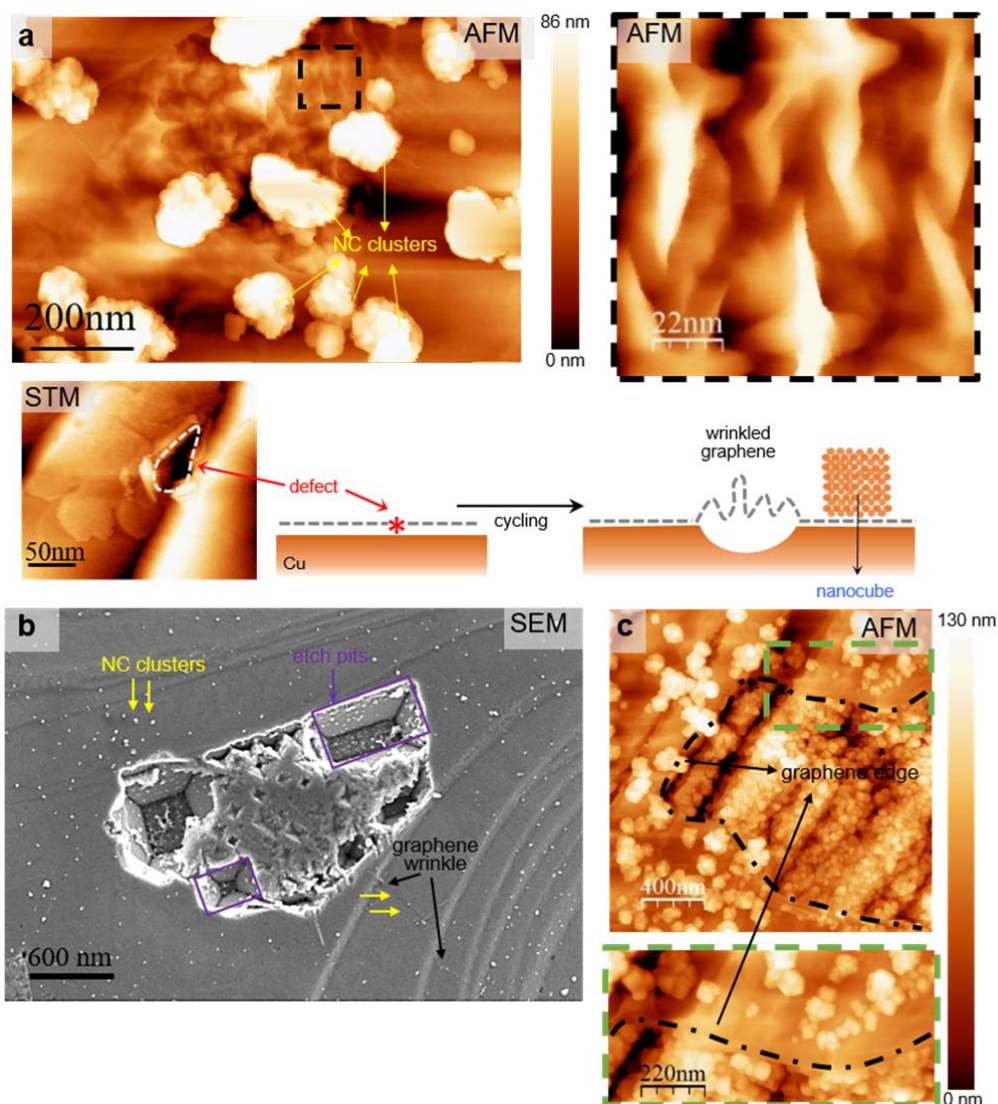
Figure 2. Micro/nanocube clusters prepared upon electrochemical cycling on g-Cu. **a**, AFM image of micro/nanocube clusters on a wrinkled graphene area together with STM image showing the area of the exposed Cu surface and unfolded graphene on pristine g-Cu. Graphene wrinkles over the shallow etch pit formed upon local dissolution of the Cu surface (see scheme). **b**, SEM image showing the micro/nanocube clusters and the etch pits on g-Cu cycled for 101 cycles. **c**, AFM images showing micro/nanocube formed on top of graphene and close to the graphene defects (here, close to the graphene edge).

When turning to the electrochemical cycling protocol, micro/nanocubes were synthesized by cycling of g-Cu in 0.1 M CO_2 saturated $KHCO_3$ (**Figure 1**.c). The protocol was modified from the methods[24] reported previously in order to prepare small NCs suitable for AFM/STM studies. After five cycles, the surface was sparsely populated with nanocubes (edge length≈ 25 nm[3]). These nanocubes are on top and weakly attached to graphene; their high mobility thus challenges AFM imaging. STM reveals that

the Cu surface underneath graphene remains flat and polycrystalline (Supplementary Figs. 3 and 4). Any changes in the cycling protocol affect micro/nanocube size and coverage, both increasing with the number of cycles (**Figure 2**). Also, the well-defined etch pits on the Cu surface formed after 101 cycles suggest that micro/nanocube formation is closely associated with Cu dissolution of uncovered areas and through graphene defects. Furthermore, the increase in the oxidation vertex potentials to the potentials higher than +0.6 V *vs* RHE resulted in the formation of micro/nanocube clusters rather than stand-alone cubes. The clusters are situated around the areas of wrinkled graphene, likely formed upon relaxation of graphene over the shallow Cu etch pit (**Figure 2**.b). Additional AFM images of cube clusters confirm that cubes preferentially form close to the graphene defects (**Figure 2**.c). Finally, no micro/nanocubes were formed when restricting the cycling potential window below the Cu dissolution potential; as in, *e.g.*, an attempt to prepare micro/nanocubes through electrochemical cycling between -0.7 and -0.2 V *vs* RHE (Supplementary Fig. 5). Taken together, these results show that cycling leads to Cu dissolution in the anodic sweep and electrodeposition of as-dissolved Cu species on top of graphene in the cathodic sweep.

Chemical composition of cuboids vs micro/nanocubes

The chemical composition of pristine Cu, g-Cu before and after in contact with the electrolyte, and nanocuboids and micro/nanocubes prepared upon constant-potential polarization and cycling were studied by quasi-*operando* XPS (**Figure 3**.a). The UHV-electrochemistry set-up[34] allows control over the atmosphere conditions during the sample preparation (conducted inside the UHV-compatible EC cell saturated with CO_2), direct sample transfer to the UHV environment, and air-free transfer to the XPS set-up.

Cu LMM Auger spectra are used to determine the occurrence of Cu^{2+}/Cu^+ species (predominant peaks at 918.4 eV, 916.5 eV, and 917.8 eV are related to metallic Cu, Cu^+ and Cu^{2+}, respectively), while the O1s spectra are employed to assess the presence of the oxygen-containing surface species. The O1s peak component centred at 532 eV (marked in grey) remained constant for all treatments; we

associate it with adsorbed H_2O/OH species[35] and surface adsorbates[36] (see AFM image in Supplementary Fig. 6) with a minor contribution from graphene defects[37,38] (consistent with the C1s spectra in Supplementary Fig. 7, showing a dominant C sp^2 peak and minor contributions from C=O and C-O). On the other hand, the O1s peaks at 530.2 eV and 529.7 eV are attributed to the presence of Cu_2O and CuO, respectively[37,39].

The pristine g-Cu sample was slightly oxidized with a dominant Cu LMM signal from metallic Cu and a minor amount of Cu_2O and CuO (Figure 3.a, red panel). Both Cu_2O and CuO components are due to Cu_xO formed upon the unavoidable local ambient oxidation of Cu, proceeded by intercalation of oxygen and water through the graphene defects, as suggested by Kwak *et al*[32]. Furthermore, the CuLMM spectrum of the g-Cu after the formation of the nanocuboids during CO_2RR displays metallic Cu with a small amount of Cu_2O (**Figure 3**.a, green panel). As the initial oxidation state can vary from sample to sample and we cannot fully discard the presence of oxygen traces during the transfer, it is important to point out that XPS/Auger analysis shows only qualitative trends, even when the measurements were performed in the exact same samples before and after the EC treatments to do meaningful comparisons. These results, together with the *operando* EC-Raman spectra discussed below, indicate that the surface remains metallic during CO_2RR but Cu_2O is rapidly formed once the sample is at open circuit potential. In agreement with AFM (Figure 1.b), STM results (Supplementary Fig. 2) and Raman spectra[12], the C1s spectrum obtained on the g-Cu sample with nanocuboids (Supplementary Fig. 7) confirms that the emergence of nanocuboids creates no additional defects in graphene and that they are fully covered by graphene. In contrast, micro/nanocubes prepared upon electrochemical cycling are mostly composed of Cu_xO (**Figure 3**.a, blue panel). Deconvolution of CuLMM spectrum reveals that micro/nanocubes on top of g-Cu have 38% Cu^0, 58% Cu_2O, and 4% CuO. Therefore, a simultaneous increase in the CuO and Cu_2O O1s components after the cycling protocol confirms the formation of Cu_xO micro/nanocubes.
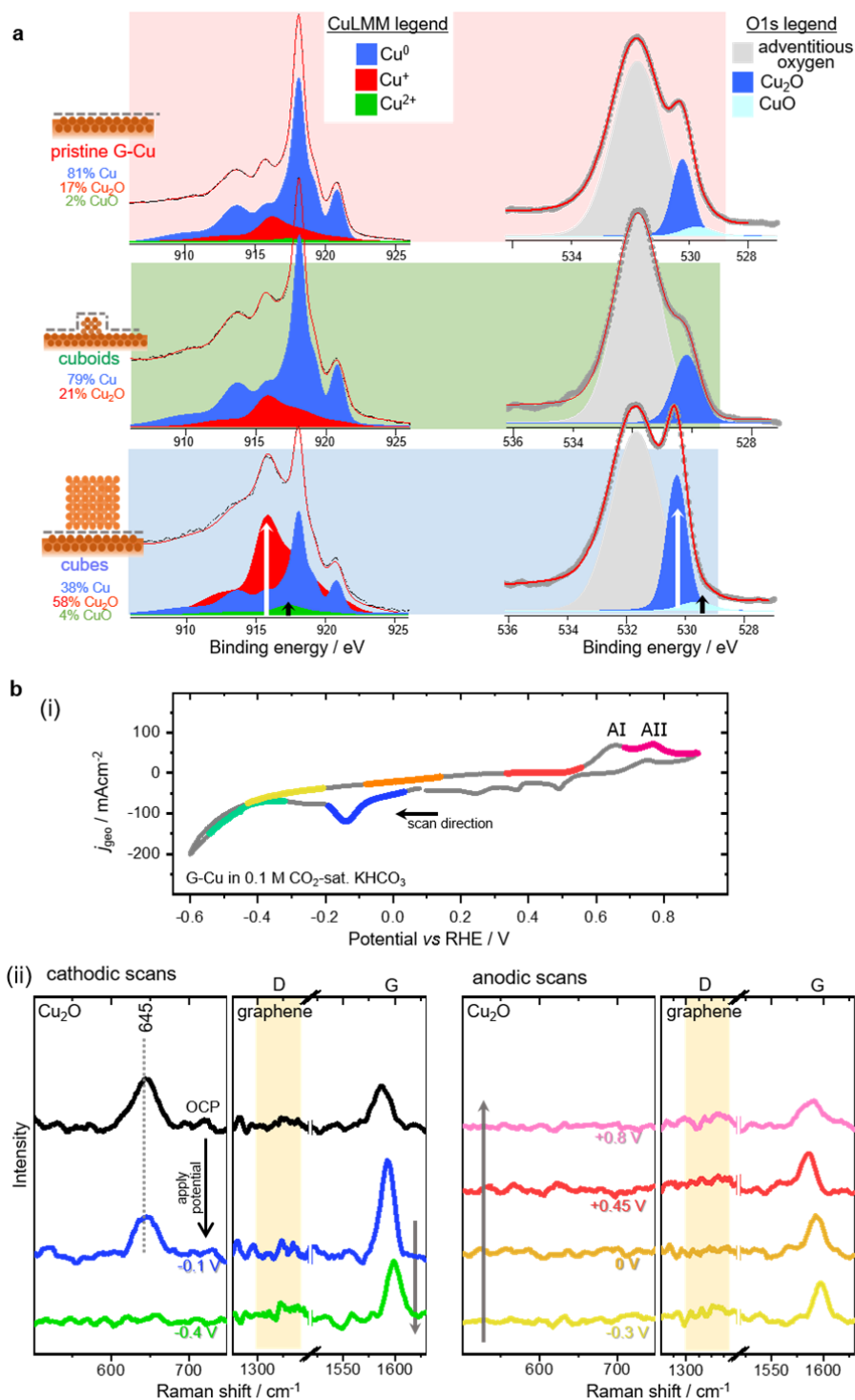
Figure 3 (Quasi-) *operando* **spectroscopy of Cu nanocubes. a**, Quasi-*operando* XPS spectra of as-received g-Cu, nanocuboids, and nanocubes. **b**, *Operando* EC Raman spectroscopy of g-Cu recorded at different potentials during cycling. (i) Cyclic voltammogram of g-Cu in 0.1 M CO_2 saturated $KHCO_3$ (pH=6.8) recorded at a scan rate of 5 mV/s. The arrow denotes the scanning direction. Different colors denote the potential ranges over which operando Raman spectra, in (*ii*), were recorded.

As a control experiment aiming to test the role of graphene on the chemical identity of nanocuboids *vs* micro/nanocubes, we performed the same experiments on polycrystalline Cu foil (Supplementary Fig. 9). The Cu surface remains mostly metallic upon *in situ* emergence of the nanocuboids during CO_2RR, while similar trends in the increase of the Cu_2O component in the O1s spectra and a decrease in the Cu/Cu^+ ratio observed after electrochemical cycling confirm differences between the chemical composition of nanocuboids *vs* micro/nanocubes.

We remark that quasi-*operando* XPS measurements were conducted under open circuit potential (OCP) conditions, *i.e.* rapid local oxidation through the graphene defects occurs. To gain further insights into the micro/nanocube formation during cycling, we tracked the changes in the chemical state of g-Cu during the first cycle using *operando* Raman spectroscopy. Characteristic Raman signatures of Cu_xO and graphene allow us to investigate simultaneously the oxidation state of Cu and the stability of graphene. Raman spectra were recorded at different potentials as g-Cu electrode was cycled in 0.1 M CO_2 saturated $KHCO_3$ between -0.6 V and +0.9 V *vs* RHE. The spectra acquired at OCP reveal the presence of the Cu_2O band (645 cm^{-1})[40,41] and the characteristic graphene G band (1585 cm^{-1})[41]. This result, together with quasi-*operando* XPS results for the g-Cu before and after the electrolyte contact (Supplementary Fig. 8–9), suggests that pristine g-Cu is slightly oxidized due to air oxidation. The reduction of the native oxide starts at the potential of ≈ 0 V *vs* RHE, while it gets fully reduced at potentials less negative than -0.2 V *vs* RHE. In the anodic scan, Cu under graphene remains metallic for potentials up to +0.9 V *vs* RHE. Simultaneous appearance of the Cu oxidation peaks (denoted as AI and AII in Figure 3.b and assigned to oxidation) suggests oxidation of Cu surface exposed through graphene defects. We also tested the oxidation behaviour of g-Cu over the wide potential range (Supplementary Fig. 10). The Cu surface under high-quality graphene remains metallic after the potential sweeps up to +1.1 V *vs* RHE.

Effect of chloride on the Cu micro/nanocube morphology

11

To investigate the role of additives on the Cu_2O micro/nanocube growth, we examined the effect of chloride. Cu_xO micro/nanocubes were prepared upon electrochemical cycling between -0.6 V and +0.9 V *vs* RHE in chloride-free 0.1 M CO_2 saturated $KHCO_3$ (Figure 4.a) and in 4 mM KCl + 0.1 M CO_2 saturated $KHCO_3$ (**Figure 4**.b). SEM was used to characterize the micro/nanocubes prepared on polycrystalline Cu foil after 100 cycles, AFM was used to visualize the micro/nanocubes prepared on g-Cu after five cycles. Cubic contours are discernable on both Cu foil and g-Cu cycled in the chloride-free electrolyte. On g-Cu, AFM reveals the smooth morphology of the underlying g-Cu and micro/nanocube clusters randomly distributed along the g-Cu substrate.
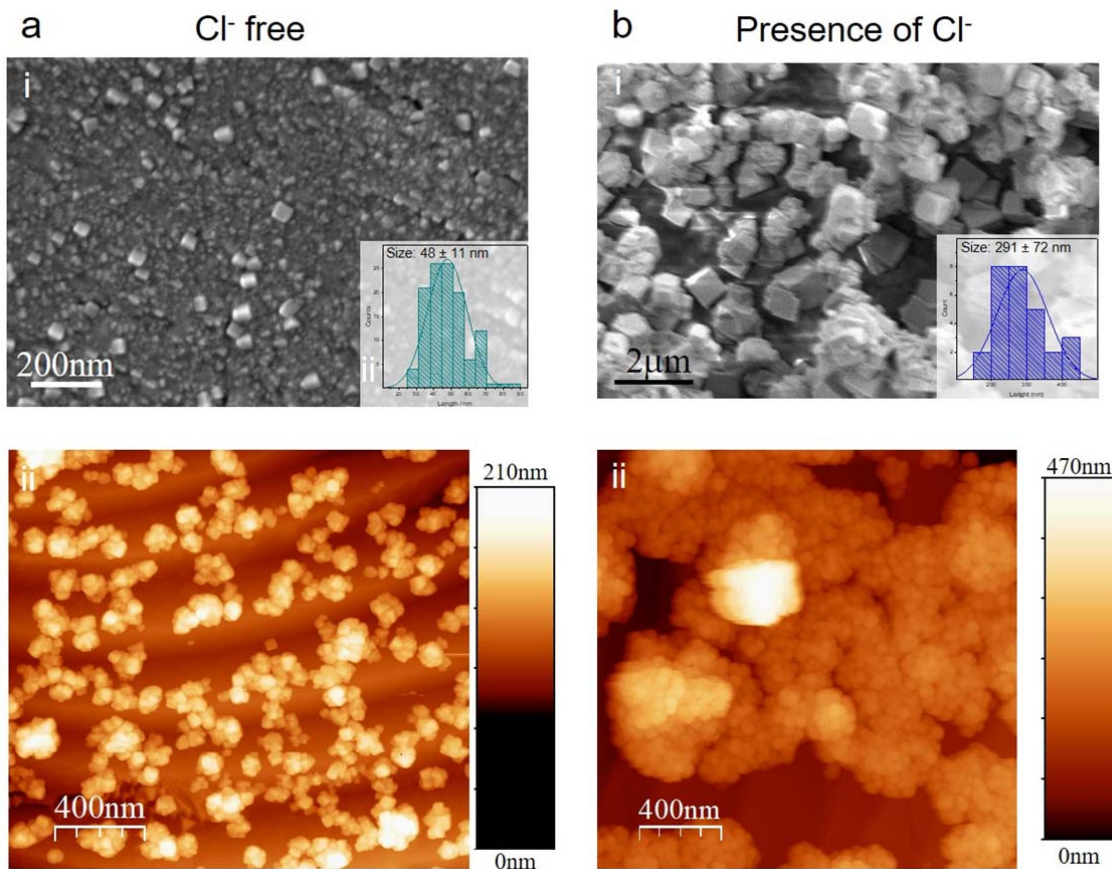
Figure 4. Effect of chloride on the Cu$_x$O micro/nanocube formation. a, Cu micro/nanocubes synthesized in a chloride-free electrolyte. (i) SEM image of Cu$_x$O micro/nanocubes prepared upon cycling of a polycrystalline Cu foil in a chloride-free electrolyte together with the corresponding size distribution. (ii) AFM image of Cu micro/nanocubes on graphene upon cycling of g-Cu. **b,** Cu$_x$O micro/nanocubes synthesized in a chloride-containing electrolyte. (i) SEM image of the Cu$_x$O micro/nanocubes prepared upon electrochemical cycling of polycrystalline Cu foil in a chloride-containing electrolyte together with the corresponding size distribution. (ii) AFM image of Cu$_x$O micro/nanocubes on g-Cu synthesized upon electrochemical cycling.

The stripping/redeposition cycling method gradually stabilizes a cubic morphology and selectively exposes the (100) facets of Cu$_2$O[24,42]. NP prepared in chloride-containing electrolytes exhibit similar structures as the ones prepared without chloride, but are six times larger. The most likely mechanism involves chloride enhancing the local dissolution of Cu, leading to the high concentration of the Cu ions close to the surface, which get electrodeposited in the cathodic scan on the graphene.

Discussion

13

The combination of electron and scanning probe microscopies characterization with *operando* spectroscopies highlights the morphological and compositional differences between Cu nanocuboids formed during CO_2RR and Cu_xO micro/nanocubes prepared upon electrochemical cycling. Moreover, we employ g-Cu as a model system that allows us to distinguish the differences in surface processes leading to the formation of metallic Cu nanocuboids underneath graphene *vs* the ones resulting in Cu_2O micro/nanocube formation on top of graphene. This approach gives an unprecedented insight into their formation mechanisms.

Cu-based CO_2RR catalysts undergo nanostructuration during CO_2RR (**Figure 5**, top panel). We highlight that nanocuboids are (100) facet multilayers (mounds) with lateral dimensions less than 100 nm. Their heights are determined by the number of the surface layers per mound, strongly dependant on the conditions of the surface prior to CO_2RR and CO_2RR conditions (electrolyte, potential, polarization time). Nanocuboids are imperceptible by SEM[43]. Moreover, they lose their square contours upon ambient oxidation and thus, appear as granular structures in post-mortem AFM and STM studies. This highlights the importance of *operando* surface-sensitive studies for understanding the *in situ* surface physics processes during CO_2RR, including nanocuboid formation as a morphological evolution occurring on all Cu electrocatalysts during CO_2RR, regardless of their microscopic precursor morphology[12,22].

14
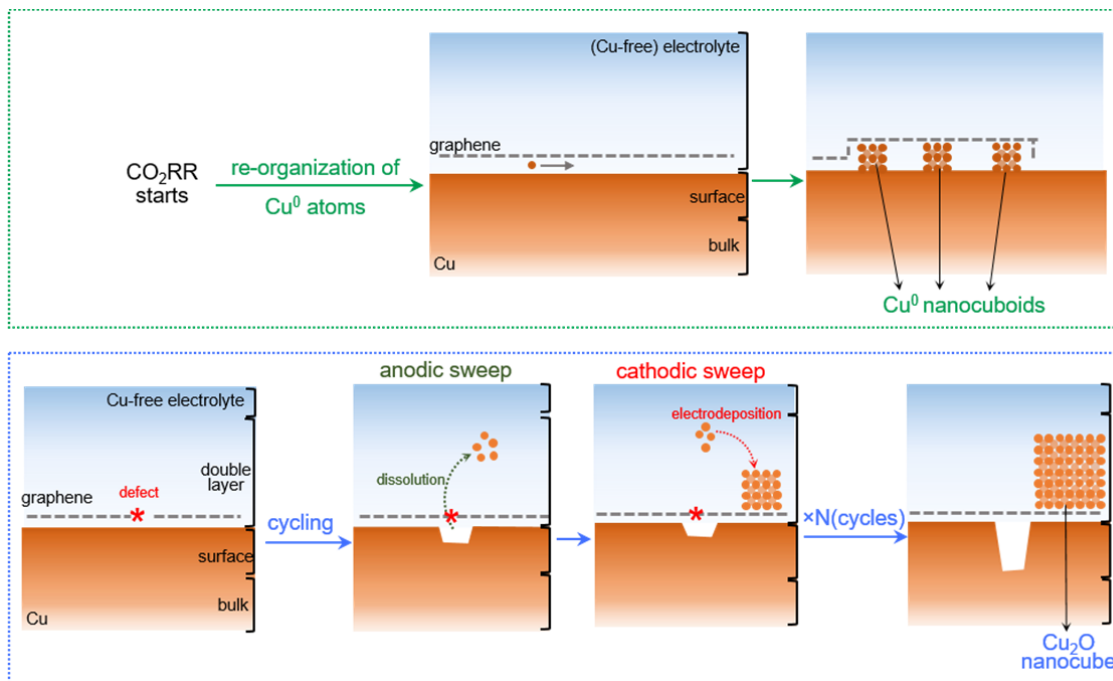
Figure 5. Formation mechanisms of the nanocuboids and micro/nanocubes. Top panel: Scheme showing the formation of the Cu nanocuboids upon potential-driven re-organization of the metallic Cu atoms during CO_2RR. Bottom panel: Scheme showing the formation of Cu_2O micro/nanocubes through sequential dissolution/electrodeposition cycles.

EC-STM, quasi-*operando* XPS (near-surface sensitive) and *operando* EC-Raman spectroscopy (deep-surface sensitive) confirm that the nanocuboids are metallic Cu(100) mounds. The native oxide, if present, is fully reduced at potentials more negative than 0 V *vs* RHE, *i.e.*, at low CO_2RR potentials[27,31]. Furthermore, our spectroscopic data allow us to discard the role of Cu^+ species on the nanocuboid formation that occurs via the re-organization of metallic Cu atoms in the top-most surface layers (**Figure 5**, top panel).[12]

When turning to the electrochemical cycling protocol, we demonstrate that the preparation of Cu_2O micro/nanocubes occurs through electrochemical cycling both in chloride-free and chloride-containing electrolytes. The observation of micro/nanocube formation in chloride-free electrolytes, together with the absence of CuCl intermediates upon cycling reported by Eilert *et al.* in chloride-containing electrolytes[44], disproves the hypothesis that CuCl determines the cubic morphology of the as-formed micro/nanocubes[20,21].

From the above results, we propose the formation mechanism of micro/nanocubes upon electrochemical cycling of Cu surfaces in Cu-ion free electrolytes (**Figure 5**, bottom panel). In the anodic sweep, the Cu surface exposed to the electrolyte through graphene defects dissolves, while Cu surface underneath graphene remains metallic. This suggests that the exposed Cu areas act as local Cu ions sources, while both graphene and Cu underneath it are electrochemically inactive. These Cu ions in the solution then get reduced and electrodeposited on top of graphene in the cathodic sweep. As-formed nuclei transform into the Cu_2O micro/nanocubes in the consecutive stripping/deposition cycles[46]. Cube morphology is thus a direct consequence of the thermodynamic stability of the Cu_2O (100) facets, where the surface energies of Cu_2O increase in the following order: $\gamma(100) < \gamma(111) < \gamma(110)$[47].

Cu dissolution at such low potentials is rather surprising. One should bear in mind that corresponding CVs appear featureless, which might be misinterpreted as if neither surface morphology nor the chemical state is changing. However, the corrosive properties of $KHCO_3$ electrolyte have been suggested earlier[48], and only a recent study shows that dissolution to Cu^+ starts at +0.5 V *vs* RHE[45]. Interestingly, dissolution occurs regardless of the local pH.

This mechanism also describes well Cu_2O micro/nanocube formation on a Cu foil. Our results suggest that the stabilization of $Cu_2O(100)$ facets upon dissolution/electrodeposition cycles seems more likely than the direct oxidation to Cu(ll) carbonate-hydroxide micro/nanocubes, which occurs upon prolonged polarization at +0.7 V *vs* RHE [44], rather than upon cycling. The same mechanism also explains the formation of Cu_xO NCs prepared upon cycling to high oxidation potentials (*e.g.*, > +0.8 V *vs* RHE in reference [45] and [49]), where Cu dissolution to Cu^{2+} ions leads to the electrodeposition in the cathodic sweeps.

Our observations rule out the need of chloride in the Cu_xO micro/nanocube formation. Chloride, often added as an additive in electrochemical cycling[25], changes the oxidation mechanism and enhances the local dissolution[50]. This strategy allows control over the Cu_xO (micro/nano)cube size

and coverage: high concentration of Cu species, here formed upon anodic dissolution of Cu surface, leads to the formation of larger cubes densely populating the substrate. However, the cubic morphology is inherent to the cycling protocols.

Conclusions

In summary, we have revealed the mechanisms of formation of Cu_2O micro/nanocubes and Cu (100) nanocuboids through two distinct *in-situ* electrosynthesis methods, namely electrochemical cycling and potential driven nanostructuration. Electrosynthesis protocols relying on cycling originate from the stripping/electrodeposition cycles, which lead to the growth of the Cu_2O nanocrystals and their evolution to micro/nanocubes. The cube morphology is a result of the thermodynamics of the crystal Cu_2O growth in the absence of any additives. Chloride anions, often added during electrosynthesis, enhance Cu dissolution in the stripping cycle, but have no role in the stabilization of the NCs. Regardless of the inital micro/nanocubic structure, under CO_2RR conditions, the oxide layer is removed and a polarization-driven nanostructuration of the surface takes place, resulting in the re-organization of the metallic Cu atoms into few nanometer-sized metallic nanocuboids. Our results highlight that a combination of the complex surface processes and electrochemical reactions occurring in the presumably safe electrochemical windows drastically change the morphologies of Cu-based catalysts. These morphological changes are imperceptible for both post-mortem and surface-insensitive spectroscopic studies, but are key to explain the trends observed in CO_2RR product selectivity that are ultimately the result of processes occurring at the atomic scale.

Methods

Samples. All experiments were performed on bare, polycrystalline Cu foils or on graphene-covered polycrystalline Cu foils (g-Cu). More details can be found in Supplementary Information.

Sample preparation: nanocuboids. Cu nanocuboids form during CO_2RR: the samples with Cu nanocuboids were thus prepared following the reference 12, *i.e.*, upon chronoamperometric polarization at -1 V vs Pt pseudo-reference electrode (-0.03 *vs* RHE) in 0.1 M CO_2 sat. $KHCO_3$ for 4 hours.

Sample preparation: micro/nanocubes. Cu_2O micro/nanocubes were prepared on g-Cu and bare Cu foils upon electrochemical cycling in 0.1 M CO_2 sat. $KHCO_3$ or 4 mM KCl/0.1 M CO_2 sat. $KHCO_3$ in a potential window between -0.6 V and +0.6 V *vs* RHE or up to +0.9 V *vs* RHE at a sweep rate of 50 mV/s for five, twenty or 101 cycles.

Morphological characterization. SEM images were acquired on Zeiss Gemini SEM using an accelerating voltage of 3 kV. AFM images were acquired in Peak Force mapping mode on Fast Scan Bio AFM (Bruker) coupled with Nanoscope Controller V and Nanoscope Software 8.15. We use FastScan-B tips (Bruker, radius of 5 nm, nominal k values of 1.8 N/m). STM characterization was carried out on the Dimension Icon STM (Bruker) coupled with the Nanoscope Controller V and Nanoscope Software 8.15 in a constant-current mode. STM and EC-STM characterization was carried out on freshly-prepared samples at room temperature.

Quasi-*operando* XPS. To minimize oxidation of the sample after electrochemical treatments, the samples characterized by XPS were prepared in the controlled environment and transferred to XPS chamber through an air-free transfer system. A home-built sample transfer system between UHV and electrochemical environment was implemented[34]. The samples were then transferred to the XPS using a vacuum suitcase (Ferrovac). The XPS measurement was conducted on a commercial Kratos AXIS Ultra system with a monochromatized Al Kα source with a base pressure in the lower range. The fitting procedure is described in the Supplementary information.

Raman spectroscopy.

Operando Raman studies were performed on an inVia Raman spectrometer (Renishaw) coupled with a confocal microscope, VersaSTAT 4 Potentiostat (Ametek), and a home-built electrochemical cell made of polytetrafluoroethylene. Raman spectra were collected using a water-immersion objective (Leica, 64×), 488 nm laser in line illumination mode, and 2400 lines/mm gratings. Line length was ≈ 12 μm; eight spectra were collected over 74.4 μm^2 area. Exposure time was 35 seconds per four spectra. The cell was equipped with a silver/silver chloride (Ag/AgCl) reference electrode immersed in 3 M NaCl solution (ProSense) and a coiled gold wire as a counter electrode. Cyclic voltammetry and linear sweep voltammetry were carried out on g-Cu samples as working electrodes (A_{geo}≈0.28cm^2). The cell was equipped with a silver/silver chloride (Ag/AgCl) reference electrode immersed in 3 M NaCl solution (ProSense) and a coiled gold wire as a counter electrode.

References

1. Nitopi, S. *et al.* Progress and Perspectives of Electrochemical CO2 Reduction on Copper in Aqueous Electrolyte. *Chem. Rev.* **119**, 7610–7672 (2019).

2. Peterson, A. A., Abild-Pedersen, F., Studt, F., Rossmeisl, J. & Nørskov, J. K. How copper catalyzes the electroreduction of carbon dioxide into hydrocarbon fuels. *Energy Environ. Sci.* **3**, 1311–1315 (2010).

3. Zhou, Y. *et al.* Dopant-induced electron localization drives CO2 reduction to C2 hydrocarbons. *Nat. Chem.* **10**, 974–980 (2018).

4. Jiao, J. *et al.* Copper atom-pair catalyst anchored on alloy nanowires for selective and efficient electrochemical reduction of CO2. *Nat. Chem.* **11**, 222–228 (2019).

5. Hori, Y., Takahashi, I., Koga, O. & Hoshi, N. Selective Formation of C2 Compounds from Electrochemical Reduction of CO2 at a Series of Copper Single Crystal Electrodes. *J. Phys. Chem. B* **106**, 15–17 (2002).

6. Loiudice, A. *et al.* Tailoring Copper Nanocrystals towards C2 Products in Electrochemical CO2 Reduction. *Angew. Chem. Int. Ed.* **55**, 5789–5792 (2016).

7. Mangione, G., Huang, J., Buonsanti, R. & Corminboeuf, C. Dual-Facet Mechanism in Copper Nanocubes for Electrochemical CO2 Reduction into Ethylene. *J. Phys. Chem. Lett.* **10**, 4259–4265 (2019).

8. Auer, A. *et al.* Self-activation of copper electrodes during CO electro-oxidation in alkaline electrolyte. *Nat. Catal.* **3**, 797–803 (2020).

9. Ledezma-Yanez, I. *et al.* Interfacial water reorganization as a pH-dependent descriptor of the hydrogen evolution rate on platinum electrodes. *Nat. Energy* **2**, 1–7 (2017).

10. Strmcnik, D. *et al.* The role of non-covalent interactions in electrocatalytic fuel-cell reactions on platinum. *Nat. Chem.* **1**, 466–472 (2009).

11. Magnussen, O. M. & Groß, A. Toward an Atomic-Scale Understanding of Electrochemical Interface Structure and Dynamics. *J. Am. Chem. Soc.* **141**, 4777–4790 (2019).

12. Phan, T. H. *et al.* Emergence of Potential-Controlled Cu-Nanocuboids and Graphene-Covered Cu-Nanocuboids under Operando CO2 Electroreduction. *Nano Lett.* **21**, 2059–2065 (2021).

13. Kim, Y.-G., Baricuatro, J. H., Javier, A., Gregoire, J. M. & Soriaga, M. P. The evolution of the polycrystalline copper surface, first to Cu(111) and then to Cu(100), at a fixed CO_2RR potential: a study by operando EC-STM. *Langmuir* **30**, 15053–15056 (2014).

14. Kim, Y.-G., Baricuatro, J. H. & Soriaga, M. P. Surface Reconstruction of Polycrystalline Cu Electrodes in Aqueous KHCO3 Electrolyte at Potentials in the Early Stages of CO2 Reduction. *Electrocatalysis* **9**, 526–530 (2018).

15. Kim, D., Kley, C. S., Li, Y. & Yang, P. Copper nanoparticle ensembles for selective electroreduction of CO2 to C2–C3 products. *Proc. Natl. Acad. Sci.* **114**, 10560–10565 (2017).

16. Huang, J. *et al.* Potential-induced nanoclustering of metallic catalysts during electrochemical CO 2 reduction. *Nat. Commun.* **9**, 3117 (2018).

17. Birdja, Y. Y. *et al.* Advances and challenges in understanding the electrocatalytic conversion of carbon dioxide to fuels. *Nat. Energy* **4**, 732–745 (2019).

18. Handoko, A. D., Wei, F., Jenndy, Yeo, B. S. & Seh, Z. W. Understanding heterogeneous electrocatalytic carbon dioxide reduction through operando techniques. *Nat. Catal.* **1**, 922 (2018).

19. Liang, Y. *et al.* Electrochemical Scanning Probe Microscopies in Electrocatalysis. *Small Methods* **3**, 1800387 (2019).

20. Roberts, F. S., Kuhl, K. P. & Nilsson, A. High selectivity for ethylene from carbon dioxide reduction over copper nanocube electrocatalysts. *Angew. Chem. Int. Ed Engl.* **54**, 5179–5182 (2015).

21. Kwon, Y., Lum, Y., Clark, E. L., Ager, J. W. & Bell, A. T. CO_2 Electroreduction with Enhanced Ethylene and Ethanol Selectivity by Nanostructuring Polycrystalline Copper. *ChemElectroChem* **3**, 1012–1019 (2016).

22. Lee, S. H. *et al.* Oxidation State and Surface Reconstruction of Cu under CO 2 Reduction Conditions from *In Situ* X-ray Characterization. *J. Am. Chem. Soc.* **143**, 588–592 (2021).

23.   Chen, C. S. *et al.* Stable and selective electrochemical reduction of carbon dioxide to ethylene on copper mesocrystals. *Catal. Sci. Technol.* **5**, 161–168 (2014).

24.   Jiang, K. *et al.* Metal ion cycling of Cu foil for selective C–C coupling in electrochemical CO 2 reduction. *Nat. Catal.* **1**, 111–119 (2018).

25.   Grosse, P. *et al.* Dynamic Changes in the Structure, Chemical State and Catalytic Selectivity of Cu Nanocubes during CO_2 Electroreduction: Size and Support Effects. *Angew. Chem. Int. Ed.* **57**, 6192–6197.

26.   Liu, H. *et al.* Scalable synthesis of hollow Cu2O nanocubes with unique optical properties via a simple hydrolysis-based approach. *J. Mater. Chem. A* **1**, 302–307 (2012).

27.   Scott, S. B. *et al.* Absence of Oxidized Phases in Cu under CO Reduction Conditions. *ACS Energy Lett.* **4**, 803–804 (2019).

28.   Lum, Y. & Ager, J. W. Stability of Residual Oxides in Oxide-Derived Copper Catalysts for Electrochemical CO2 Reduction Investigated with 18 O Labeling. *Angew. Chem. Int. Ed Engl.* **57**, 551–554 (2018).

29.   Eilert, A. *et al.* Subsurface Oxygen in Oxide-Derived Copper Electrocatalysts for Carbon Dioxide Reduction. *J. Phys. Chem. Lett.* **8**, 285–290 (2017).

30.   De Luna, P. *et al.* Catalyst electro-redeposition controls morphology and oxidation state for selective carbon dioxide reduction. *Nat. Catal.* **1**, 103–110 (2018).

31.   Löffler, M., Mayrhofer, K. J. J. & Katsounaros, I. Oxide Reduction Precedes Carbon Dioxide Reduction on Oxide-Derived Copper Electrodes. *J. Phys. Chem. C* **125**, 1833–1838 (2021).

32.   Kwak, J. *et al.* Oxidation behavior of graphene-coated copper at intrinsic graphene defects of different origins. *Nat. Commun.* **8**, 1549 (2017).

33.   Arán-Ais, R. M., Scholten, F., Kunze, S., Rizo, R. & Roldan Cuenya, B. The role of in situ generated morphological motifs and Cu(i) species in C2+ product selectivity during CO2 pulsed electroreduction. *Nat. Energy* **5**, 317–325 (2020).

34. Grumelli, D., Wurster, B., Stepanow, S. & Kern, K. Bio-inspired nanocatalysts for the oxygen reduction reaction. *Nat. Commun.* **4**, 1–6 (2013).

35. Andersson, K. *et al.* Bridging the Pressure Gap in Water and Hydroxyl Chemistry on Metal Surfaces: The Cu(110) Case. *J. Phys. Chem. C* **111**, 14493–14499 (2007).

36. Li, Z. *et al.* Effect of airborne contaminants on the wettability of supported graphene and graphite. *Nat. Mater.* **12**, 925–931 (2013).

37. Kidambi, P. R. *et al.* Observing Graphene Grow: Catalyst–Graphene Interactions during Scalable Graphene Growth on Polycrystalline Copper. *Nano Lett.* **13**, 4769–4778 (2013).

38. Álvarez-Fraga, L. *et al.* Oxidation Mechanisms of Copper under Graphene: The Role of Oxygen Encapsulation. *Chem. Mater.* **29**, 3257–3264 (2017).

39. Biesinger, M. C. Advanced analysis of copper X-ray photoelectron spectra. *Surf. Interface Anal.* **49**, 1325–1334 (2017).

40. Deng, Y., Handoko, A. D., Du, Y., Xi, S. & Yeo, B. S. In Situ Raman Spectroscopy of Copper and Copper Oxide Surfaces during Electrochemical Oxygen Evolution Reaction: Identification of CuIII Oxides as Catalytically Active Species. *ACS Catal.* **6**, 2473–2481 (2016).

41. Yin, X. *et al.* Evolution of the Raman spectrum of graphene grown on copper upon oxidation of the substrate. *Nano Res.* **7**, 1613–1622 (2014).

42. Yang, J., Wan, X., Tie, S., Lan, S. & Gao, X. Crystal-facet-controllable synthesis of Cu2O micron crystals by one-step, surfactant- and capping agent-free method and the formation mechanism. *Solid State Sci.* **104**, 106203 (2020).

43. Wang, Y. *et al.* Catalyst synthesis under CO 2 electroreduction favours faceting and promotes renewable fuels electrosynthesis. *Nat. Catal.* **3**, 98–106 (2020).

44. Eilert, A., Roberts, F. S., Friebel, D. & Nilsson, A. Formation of Copper Catalysts for CO_2 Reduction with High Ethylene/Methane Product Ratio Investigated with In Situ X-ray Absorption Spectroscopy. *J. Phys. Chem. Lett.* **7**, 1466–1470 (2016).

45.   Speck, F. D. & Cherevko, S. Electrochemical copper dissolution: A benchmark for stable CO2

reduction on copper electrocatalysts. *Electrochem. Commun.* **115**, 106739 (2020).

46.   Arán-Ais, R. M. *et al.* Imaging electrochemically synthesized Cu 2 O cubes and their

morphological evolution under conditions relevant to CO 2 electroreduction. *Nat. Commun.* **11**,

3489 (2020).

47.   Huang, W.-C., Lyu, L.-M., Yang, Y.-C. & Huang, M. H. Synthesis of Cu2O nanocrystals from

cubic to rhombic dodecahedral structures and their comparative photocatalytic activity. *J. Am.*

Chem. Soc. **134**, 1261–1267 (2012).

48.   Pérez Sánchez, M. *et al.* A mechanistic approach to the electroformation of anodic layers on

copper and their electroreduction in aqueous solutions containing NaHCO3 and Na2CO3.

Electrochimica Acta **38**, 703–715 (1993).

49.   Tang, W. *et al.* The importance of surface morphology in controlling the selectivity of

polycrystalline copper for CO2 electroreduction. *Phys. Chem. Chem. Phys.* **14**, 76–81 (2012).

50.   Marcus, P., Maurice, V. & Strehblow, H.-H. Localized corrosion (pitting): A model of passivity

breakdown including the role of the oxide layer nanostructure. *Corros. Sci.* **50**, 2698–2704 (2008).

Acknowledgements

Author contributions

K.B., T.-H.P., and M.L. conceived and designed the experiments. R.G. and M.L. supervised the project and led the collaboration efforts. K.B., T.-H.P., and P.A. carried out experiments and obtained the data. The experimental data was analyzed by K.B., F.P.C., R.G., Y.L., and M.L. and discussed by all the authors. The manuscript was written by K.B. and M.L. with contributions from all the authors.

Competing interests

The authors declare no competing financial interests.

Additional information